

Blade-resolved numerical simulations of the NREL offshore 5 MW baseline wind turbine in full scale: a study of proper solver configuration and discretization strategies

de Oliveira, M. a,*^a, Puraca, R. C. a^a, Carmo, B. S. a^a

^a*University of São Paulo, Escola Politécnica, Dept. of Mechanical Engineering, Brazil.*

Abstract

This paper presents a blade-resolved numerical investigation of the NREL 5 MW baseline wind turbine for offshore applications including blade-tower interference, analyzing the solver configuration and its influence on the results accuracy and computational costs. The wind turbine was analyzed considering its full dimensions under the operating condition of optimal wind-power conversion efficiency for a wind speed of 10 m/s at hub height. The power production, generated thrust, and forces distribution along the blade span were estimated. The computational analyses were carried out using a Computational Fluid Dynamics (CFD) methodology employing the Finite Volume Method (FVM) implemented in the OpenFOAM software considering different approaches of the Pressure Implicit Split Operator (PISO) solver and different mesh refinement strategies for the spatial discretization process, which resulted in two different meshes being investigated. For one of the meshes, a temporal discretization analysis was performed for three different CFL numbers. The iterative form of the PISO algorithm was considered in its generic form and with an extra step to correct the pressure before the beginning of the iterative process in each time step. Both approaches can be accomplished in OpenFOAM through the PIMPLE solver facilities for the treatment of the pressure-velocity coupling in unsteady problems. The analysis of the transient incompressible turbulent flow was conducted considering the same turbulence model for all CFD investigations, the URANS $k - \omega$ SST. A numerical verification was conducted in each analysis by comparing the CFD results against values obtained using the blade element momentum theory, implemented in OpenFAST. To conclude each analysis, a computational cost investigation was carried out. Finally, for the spatial and temporal discretization investigation, detailed information regarding the flow characteristics is presented. According to the accuracy of the results obtained through the CFD simulations, the best numerical arrangement is given by the iterative PISO with face flux correction as pressure-based solver and a temporal discretization which employs lower values of CFL, such as 1 or 2.

Keywords: NREL 5 MW Wind Turbine, Blade-resolved Simulations, Iterative PISO Solver, Spatial and Temporal investigations, Computational Cost Analysis.

1. Introduction

Motivated by environmental issues such as global warming and air pollution, the use of renewable energy sources has become a relevant strategy to avoid these unfavorable impacts [1, 2]. One of the options is wind energy, which has developed into a mainstream source of electricity due accelerated technology development and increase of productivity with scale. These aspects

also led to the expansion of wind energy to offshore areas, which can present outstanding wind resources [3, 4].

However, the growth in number and size of wind turbines does not come without challenges. The environment in which the wind turbines operate include atmospheric boundary layer and turbulence effects which vary spatially. Moreover, the substantial increase in the size of the commercial wind turbines due to the economy of scale, and the wind turbine blades-tower interaction, result in several uncertainties regarding the aerodynamic loads prediction and wake behavior. Therefore, considering that the cost associated with offshore instal-

*Corresponding author
Email address: marielledeoliveira@usp.br (de Oliveira, M.)

Nomenclature

AMI	Arbitrary Mesh Interface	$\overline{\mathbf{U}'\mathbf{U}'}$	Reynolds stress tensor
CFD	Computational Fluid Dynamics	ϕ	Generic variable
CFL	Courant-Friedrichs-Lowy	τ_1, τ_2	Time-scales
DES	Detached Eddy Simulation	\mathbf{N}	Control Volume \mathbf{N} , neighbors of Control Volume \mathbf{P}
FVM	Finite Volume Method	\mathbf{P}	Control Volume \mathbf{P}
HAWT	Horizontal Axis Wind Turbines	\mathbf{U}	Velocity vector
LES	Large Eddy Simulation	\mathbf{U}_f	Control volume velocity at the face cell
N-S	Navier Stokes	\mathbf{U}_p	velocity at the centre of the cell
NASA	National Aeronautics and Space Administration	\mathbf{d}	Distance between cell center of the volume control of interest denominated by \mathbf{P} , and its neighboring cell centre
NREL	National Renewable Energy Laboratory	\mathbf{f}	Surface tension and body forces
OWTs	Offshore Wind Turbines	\tilde{P}_k	Production limiter of specific kinetic energy
PISO	Pressure Implicit Split Operator	a_N	Interpolation coefficient at the faces of the control volume \mathbf{N}
SIMPLE	Semi-Implicit Method for Pressure-Linked Equations	a_P	Interpolation coefficient at the faces of the control volume \mathbf{P}
SIMPLEC	Semi-Implicit Method for Pressure-Linked Equations Consistent	h_o	Reference height
SST	Shear Stress Transport	k	Turbulent kinetic energy
UAE	Unsteady Aerodynamic Experiment	k^+	Dimensionless turbulent kinetic energy
URANS	Unsteady Reynolds-Average Navier-Stokes	p	Kinematic pressure
WT	Wind Turbine	u_τ	Friction velocity
Co	Courant number	y	Height variation
P_k	Production of specific kinetic energy	y^+	Dimensionless wall distance
Re_L	Reynolds number	z_0	Roughness height
Δt	Time step	F	Mass flux through a general face
ϵ	Specific rate of dissipation of turbulent kinetic energy	H	Tower height
κ	von Kármán constant	R	Blade radius
ν	Kinematic viscosity	S	Area vector pointing out of the volume cell
ν_t	Eddy viscosity	t	Time
ν_t	Kinematic eddy viscosity		
ω	Turbulence frequency		

lations are superior, the need of better numerical codes to accurately predict the offshore wind turbine loads in the design phase become more important.

To date, few experimental campaigns have been performed to quantify the unsteady three-dimensional aerodynamic behaviour of horizontal-axis wind turbines (HAWT), such as the National Renewable Energy Laboratory (NREL) test reported in [5], where aerodynamic loads of a 10 m rotor of a two-bladed, downwind turbine were evaluated in an outdoor field under several environmental conditions, and the other NREL test reported in [6], in which an Unsteady Aerodynamic Experiment (UAE) of a heavily instrumented 20-kW HAWT, placed inside the world's largest wind tunnel at NASA's Ames Research Center, was carried out under homogeneous conditions, almost no blockage effects and an equivalent Reynolds number of approximately one million. The tests were able to provide high-quality data which have shown that HAWT undergoes significantly complex aerodynamic loads and that 3D effects are prevalent. Even though the tests were able to provide important data which have been used to validate and enhance engineering models, due to the ever increasing power capacity of offshore wind turbines (OWT), for instance, the Robin Rigg wind farm comprises 58 OWT of 3 MW, Block Island wind farm consists of 5 OWT of 6 MW each, and the Thorntonbank wind farm is composed by 54 6.15 MW OWT [7]), the development of more robust numerical models capable of considering these three-dimensional effects in the design phase to better predict the OWT performance is necessary [6, 8]. Among the numerical approaches in which such effects are taking into account, the CFD technique has been shown to be a mature, promising and reliable method to investigate the unsteady aerodynamic behavior of the flow around wind turbine blades and wakes generated [9, 10].

Up to now, since the first blade-resolved simulation of a wind turbine rotor blade [11], an extensively number of CFD investigations regarding rotor-only simulations have been made, such as for the NREL Phase II rotor [12], the NREL Phase VI rotor [13] and for the MEXICO rotor [8]. Previous investigations also showed that it is yet not feasible to resort to direct numerical simulations (DNS) to analyse wind turbine performance, so the numerical solution of the Navier-Stokes equations requires special treatment of turbulence, either by making use of Unsteady Reynolds-Average Navier-Stokes (URANS) turbulence models [14, 15], by performing Large Eddy Simulations (LES) [16], or by adopting a hybrid approach, called Detached Eddy Simulation (DES) [17]. According to [8], the URANS model is sufficient to predict the flow correctly when the flow is fully

attached, whereas for considerably separated flow, the DES model has been put forward as a promising solution in the rotor-only investigations since it improves the accuracy with less computational cost than LES [18].

However, when considering the blades, nacelle and tower geometries of a megawatt-scale turbine in CFD investigations, more effort to optimize the computational cost, while achieve accurate results with the numerical modeling must be made. For example, in the investigations performed by [16], the quasi-steady regime for the power and thrust, which typically requires around 5-6 rotor revolutions to be established, was not achieved even for the coarsest mesh. The results considering only 3 revolutions were compared with the reduced-order wind turbine simulation tool NREL's FAST code [19], and differences of around 6% for power and 20% for thrust were observed. To perform the numerical investigations, the authors considered as turbulence model the hybrid DES approach, which due to the mesh strategy employed, presented a high computational demand. Considering that to investigate the wind turbine performance, the flow around the blades is modeled with an URANS approach even in the hybrid DES turbulence model, this work only considers the URANS model to deal with turbulence in order to reduce the computational cost and to be able to predict the power and thrust considering the operational steady state.

Different URANS turbulence model options were tested by other authors to simulate the flow field around a HAWT blade, such as one-equation [20], and two-equations [15, 21] models. Tests performed by [22] showed that the Spalart-Allmaras one-equation model was less sensitive in the near wall region in representing the viscosity effects in the boundary-layer, and between the two-equations models, the standard $k - \varepsilon$ has shown to be inadequate for the aerodynamics loads evaluation of HAWT blades. On the other hand, the Shear Stress Transport (SST) $k - \omega$ model from [23] is vastly recommended for the prediction of aerodynamic forces of wind turbine blades in 3D investigations [15], presenting good agreement with experimental results such as those from the MEXICO project [24], and from the NREL Phase VI test [25].

Besides the turbulence model, there are other important factors to be considered during the CFD investigation of a HAWT, which impact directly in the simulation convergence and computational cost of such analysis. For instance, regarding the solver considered to predict the flow behaviour, since the compressibility effect which occurs at the blade tip of large wind turbines can be neglected [26], the flow is treated as incompressible

through a pressure-based solver. The treatment of the pressure-velocity coupling problem in transient incompressible flows results in a large set of algebraic equations and an iterative approach is required to segregate the dependent variables and the governing equations being solved in a sequential manner [27]. Therefore, the basic form of the solution algorithm remains the same even with the inclusion of time dependence, turbulence and other transport equations. Regarding the difficulty related to the pressure determination, [28] suggested a solution for the segregated method based on staggered grids in which velocity and pressure are estimated at different points of the cell to stabilize the solver convergence.

Among the solver algorithms options to obtain a segregated solution, the different forms of the Pressure Implicit with Splitting of Operators (PISO) [29], and the Semi-Implicit Method for Pressure-Linked Equations (SIMPLE) [30] algorithms are the most common and recommended methods to solve the pressure-velocity coupling problem in incompressible flow investigations. A variety of the PISO and SIMPLE algorithms has been employed in the numerical investigation of wind turbines [10, 31–33]. Both algorithms present different attractive alternatives, the better option is the one which works in balance with the computational demand and the accuracy required for the problem being investigated. According to [34], the non-iterative PISO algorithm, which was developed initially by [29] to solve unsteady transient flows, has been successfully adapted for iterative solutions involving the pressure-velocity calculations. In addition, the iterative methods play a crucial role to achieve convergence in problems involving dynamic mesh [35], which requires special treatment such as the Arbitrary Mesh Interface (AMI) technique, which is the method considered in the investigations presented in this work.

In OpenFOAM, the iterative form of the PISO algorithm is achieved through the PIMPLE solver utility by changing the parameter nCorrector from 1 to 2 in the simulation control dictionary. The iterative approach is advantageous as it includes an outer loop correction for the iterative process and a second correction for the pressure is performed before going to the next time step. The modeling performed in the present investigations considered a dynamic mesh and the transient analysis were solved considering the iterative approach of the PISO algorithm, which is presented in details in the next section.

Last but not least, according to Jasak [36], the boundedness of the solution for diagonally equal systems of equations will be preserved only for matrices which

present positive coefficients. Therefore, in order to provide the required condition that make the solver to work correctly, attention regarding the spatial discretization such as the non-orthogonality of the mesh, which can be treated through the source term by considering the appropriate corrections, is necessary. In this work, besides the non-orthogonality correction, an extra correction for the flux which cross the mesh cell's face is also considered to verify its influence in the accuracy of the results and computational cost.

Heretofore, the reported blade-resolved simulations of a megawatt scale wind turbine, such as the NREL 5 MW, focused primarily on the determination of the wind turbine performance by modeling the multi-physical problem. For example, we can find works on fluid-structure interaction analysis [37, 38] and aerodynamics performance considering the pitch angle variation and the aero-hydrodynamic coupled problem [39–41]. However, in all investigations the solver is presented, but no investigation regarding the influence of the solver parameters on the accuracy of the results or computational costs are analyzed. With the increase in the wind turbines power to values of the order of 15 MW, the numerical modeling in full scale becomes even more challenging, and the need of a optimized solver more evident. Therefore, in order to cover these needs, the target of this paper is to present a methodology based on a solver investigation to perform blade-resolved CFD simulations to adequately predict the aerodynamic loads and the overall wind turbine performance considering the baseline NREL 5 MW wind turbine for offshore applications in full scale, under operating condition of optimal wind-power conversion efficiency. These simulations are computationally expensive and challenging to set up and converge, so we hope the discussion and results we will present in the next sections will help in the modeling and simulation of other large wind turbines. The access to the entire flow field may be very valuable to comprehend the physics and improve the performance of wind turbines, and this might have a huge social and economical impact, given the accelerated growth that is predicted for offshore wind energy in the coming decades.

2. Methodology

To perform the numerical investigations, two different spatial discretization strategies were considered. For the first mesh being analyzed, Mesh-1, an extra face flux correction was considered and its good performance made us to also employ it in the analyses carried out

with the second mesh being investigated, Mesh-2. After comparing the results among the two different spatial discretization strategies, Mesh-2 was selected as the most suitable one when considering the balance between results accuracy and computational cost. At last, for Mesh-2 a time discretization investigation was performed considering different Courant-Friedrichs-Lowy (CFL) numbers, with the purpose of analyzing the influence of this convergence parameter in the results accuracy and computational cost.

The investigations were carried out considering the three-dimensional URANS approach and the $k - \omega$ SST turbulence model. As a verification procedure, the CFD results were benchmarked against the results obtained with OpenFAST [42], which implements the blade element momentum method, considering the same NREL 5 MW wind turbine at the same environmental conditions.

The remainder of this section is dedicated to describe the governing equations considered to model the problem and also the solver algorithm employed in each CFD investigation.

2.1. Governing Equations

Considering the problem being investigated, the governing set of equations is composed by the conservation of mass and conservation of momentum equations, given respectively by:

$$\nabla \cdot \mathbf{U} = 0, \quad (1)$$

$$\frac{\partial \mathbf{U}}{\partial t} + \nabla \cdot (\mathbf{U}\mathbf{U}) = -\nabla p + \nabla \cdot (\nu \nabla \mathbf{U}) + \mathbf{f}, \quad (2)$$

where t is time, ν is the kinematic viscosity, \mathbf{U} is the velocity vector, p is the kinematic pressure and \mathbf{f} represents the body forces.

2.2. Discretization of the governing equations by the Finite Volume Method (FVM)

In this section the governing equations are discretized through the FVM in order to highlight the aspects which require special attention, such as the non-linearity of the momentum equation and the linear dependence between velocity and pressure. Detailed information regarding the FVM can be found in [28]. The discretisation of the non-linear term given by the convective term in Eq. (2) by the FVM leads to

$$\nabla \cdot (\mathbf{U}\mathbf{U}) = \sum_f \mathbf{S}(\mathbf{U}_f)(\mathbf{U}_f) = \sum_f F(\mathbf{U}_f), \quad (3)$$

$$\nabla \cdot (\mathbf{U}\mathbf{U}) = a_P \mathbf{U}_P + \sum_N a_N \mathbf{U}_N, \quad (4)$$

where \mathbf{S} is the area vector pointing out of the volume cell with magnitude equal to the face area, F represents the term $\mathbf{S} \cdot (\rho \mathbf{U})_f$, which is the mass flux through a general face, whereas \mathbf{U}_f is the control volume velocity at the face cell. The coefficients a_P and a_N are related to the values interpolated at the faces of the control volume P and its neighbors indicated by N , and are functions of the velocity \mathbf{U} . The same goes for F , which must satisfy the continuity equation. Because of the complexity of the non-linear solvers and the computation effort required, a linearisation of the convective term is recommended. Considering the type of flow being investigated, and following the recommendations by [34] and [36], the calculation of the F term is performed using an upwind numerical method to guarantee the boundedness of the solution by preserving positive coefficients in the linear algebraic equation matrices.

To discretize the kinematic pressure term in the Eq 2, a semi-discrete form of the momentum equation is considered,

$$a_P \mathbf{U}_P = \mathbf{H}(\mathbf{U}) - \nabla p, \quad (5)$$

where \mathbf{U}_P is the velocity at the centre of the cell, $\mathbf{H}(\mathbf{U})$ consists of the sum of the transport and source parts, as in

$$\mathbf{H}(\mathbf{U}) = - \sum_N a_N \mathbf{U}_N + \frac{\mathbf{U}}{\Delta t}, \quad (6)$$

where Δt is the time step.

The discretized form of the continuity equation, Eq. (1), is given by

$$\nabla \cdot \mathbf{U} = \sum_f \mathbf{S} \mathbf{U}_f = 0. \quad (7)$$

The velocity at the centre of the cell of interest is obtained by considering Eq. 5, resulting in

$$\mathbf{U}_P = \frac{\mathbf{H}(\mathbf{U})}{a_P} - \frac{1}{a_P} \nabla p. \quad (8)$$

In addition, by considering Eq. 8, the velocity at the cell face, which is necessary for the calculation of the fluxes, is expressed by

$$\mathbf{U}_f = \left(\frac{\mathbf{H}(\mathbf{U})}{a_P} \right)_f - \left(\frac{1}{a_P} \right)_f (\nabla p)_f. \quad (9)$$

The pressure equation is obtained by substituting Eq. (9) into the discretized form of the continuity given by Eq. (7). Hereby, the discretized form of the kinematic pressure term is given by

$$\nabla \cdot \left(\frac{1}{a_P} \right) = \nabla \cdot \left(\frac{\mathbf{H}(\mathbf{U})}{a_P} \right) = \sum_f \mathbf{S} \left(\frac{\mathbf{H}(\mathbf{U})}{a_P} \right)_f. \quad (10)$$

Finally, the discretized form of the incompressible Navier-Stokes equations are given by

$$a_P \mathbf{U}_P = \mathbf{H}(\mathbf{U}) - \sum_f \mathbf{S}(p)_f, \quad (11)$$

$$\sum_f \mathbf{S}\left[\left(\frac{1}{a_P}\right)_f (\nabla p)_f\right] = \sum_f \mathbf{S}\left(\frac{\mathbf{H}(\mathbf{U})}{a_P}\right)_f, \quad (12)$$

with the calculation of the face fluxes F given by

$$F = \mathbf{S}\mathbf{U}_f = \mathbf{S}\left[\left(\frac{\mathbf{H}(\mathbf{U})}{a_P}\right)_f - \left(\frac{1}{a_P}\right)_f (\nabla p)_f\right]. \quad (13)$$

It is important to notice that in the discretized form of the Navier-Stokes set of equations given, Eqs. (11) and (12), a linear simultaneous dependence between velocity and pressure is observed. To handle this inter-equation coupling problem, special treatment is required.

2.3. Pressure-velocity coupling problem

Since the flow is incompressible, the density is constant inducing a lack of one equation to estimate the pressure field directly. The pressure can be interpreted as a Lagrange multiplier that enforces the velocity field to be divergence-free, which is equivalent to obey the mass conservation equation. As recommended by [28], for a segregated solution, the mass flow rate across the cell faces is given by the aforementioned variable F , which can be estimated without any interpolation process. Based on [34] and [36], the pressure-based solver chosen to perform the CFD investigations was the iterative form of the PISO algorithm which can be implemented in OpenFOAM through the PIMPLE solver utility. By changing the setup of this solver, it is possible to obtain a variety of pressure-based algorithms such as the non-iterative and the iterative PISO, transient SIMPLE, SIMPLEC and others [10]. The iterative PISO solver is an attractive option since for each time step the algorithm solves the pressure corrections twice in an iterative approach to reach the desired tolerance. In the investigations conducted for our Mesh-1, an extra correction for the F term was aggregated to the iterative PISO solver and tested to verify its influence in the accuracy of the results and associated computational cost. A detailed information regarding the algorithm sequence solved in each time step is presented in Fig. 1 for the two approaches which were tested. It is possible to notice that when considering the face flux correction an extra correction for the pressure is performed before the start of the iterative PISO steps.

2.4. Temporal discretisation scheme

The choice for the time-integrator scheme depends on the type of equations being solved [36]. In this work we employ an implicit second order upwind Euler scheme to achieve a better accuracy in time marching. The temporal discretisation is carried out through the Backward scheme [43], in which the information from the current and previous time step is stored. The discretised form of the temporal derivative is obtained by considering the Taylor series expansion of a variable Φ in time around the new value of Φ as $\Phi(t + \Delta t) = \Phi^a$ as in

$$\Phi(t) = \Phi^b = \Phi^a - \frac{\partial \Phi}{\partial t} \Delta t + \frac{1}{2} \frac{\partial^2 \Phi}{\partial t^2} \Delta t^2 + O(\Delta t^3). \quad (14)$$

Therefore, the temporal derivative discretized term in a first-order accuracy is given by,

$$\frac{\partial \Phi}{\partial t} \Delta t = \frac{\Phi^a - \Phi^b}{\Delta t} + O(\Delta t^2). \quad (15)$$

To achieve second-order accuracy, the additional Taylor series term from the previous time step must be considered. This relation is given by

$$\Phi(t - \Delta t) = \Phi^c = \Phi^a - 2 \frac{\partial \Phi}{\partial t} \Delta t + 2 \frac{\partial^2 \Phi}{\partial t^2} \Delta t^2 + O(\Delta t^3). \quad (16)$$

In order to eliminate the truncation error with the scale of Δt , the Backward scheme combines Eqs. (14) and (16), so the second order approximation of the temporal derivative is obtained:

$$\frac{\partial \Phi}{\partial t} = \frac{\frac{3}{2} \Phi^a - 2 \Phi^b + \frac{1}{2} \Phi^c}{\Delta t}, \quad (17)$$

where Φ is the variable being calculated, Δt is the time step, and the coefficients a , b and c are given by

$$a = 1 + \frac{\Delta t}{\Delta t + \Delta t_b}, \quad (18)$$

$$c = \Delta t \times \frac{\Delta t}{\Delta t_b \times (\Delta t + \Delta t_b)}, \quad (19)$$

$$b = a + c. \quad (20)$$

As usually, in this work the stability of the temporal discretization method was limited by the Courant number,

$$Co = \frac{\mathbf{U}_f \Delta t}{|\mathbf{d}|}, \quad (21)$$

where as aforementioned \mathbf{U}_f is the control volume velocity at the face cell, Δt is the time step and \mathbf{d} is the vector that represents the distance between the cell center of

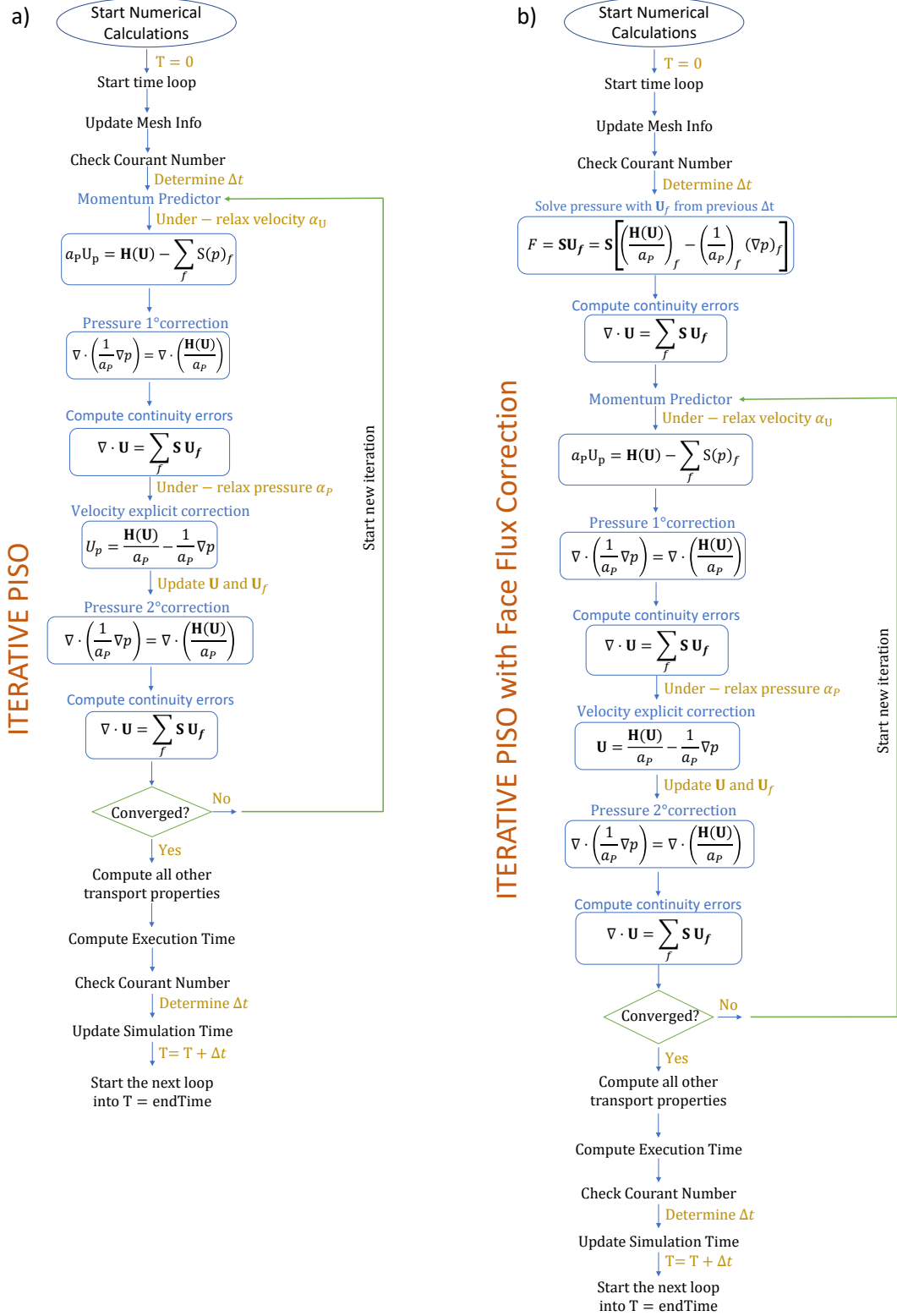


Figure 1: Iterative PISO algorithm steps considered in the numerical investigation. a) Generic form, b) With face flux correction.

the control volume of interest denominated by P , and its neighboring cell centre. Therefore, the Courant number represents a measure of the information quantity being carried, which transverses a volume cell of the mesh in a given time step. It is worth mentioning that the CFL refers to the maximum allowable Courant number that a certain time-integrator scheme can employ. Usually, explicit methods have CFL condition close to the unit, while for implicit schemes the parameter can be larger than 1 as it is less sensitive to numerical instabilities [34].

In the numerical investigations of our Mesh-2, different CFL numbers were considered in order to understand the sensitivity of the results and computational cost with respect to this parameter.

2.5. Turbulence Modeling

Finally, by considering the appropriated additional set of transport equations to represent the turbulence model, an approximate solution for the Navier-Stokes set of equations can be obtained. An ideal turbulence model should minimize the complexity of the flow field in order to capture the features of the most significant part of the system physics [44]. For the reasons already mentioned in the introduction, here we employ the URANS method which is a statistical procedure applied to the Navier-Stokes equations. By taking the average of the N-S equations, the closure problem arises, i.e. there are not enough equations to solve the nonlinear Reynolds stress tensor term. This gives rise to the turbulence models which are necessary to close the set of equations of the URANS model.

The incompressible URANS equations are obtained by means of average decomposition. Applying the averaging procedure into the continuity equation and incompressible Navier-Stokes equations given respectively by Eqs. (3) and (4), the averaged form of the equations are obtained:

$$\nabla \cdot \bar{\mathbf{U}} = 0, \quad (22)$$

$$\frac{\partial \bar{\mathbf{U}}}{\partial t} + \nabla \cdot (\bar{\mathbf{U}} \bar{\mathbf{U}}) = -\nabla \bar{p} + \nabla \cdot (\nu \nabla \bar{\mathbf{U}}) + \mathbf{f} + \bar{\mathbf{U}}' \bar{\mathbf{U}}'. \quad (23)$$

where all the terms were explained previously except the term $\bar{\mathbf{U}}' \bar{\mathbf{U}}'$ which represents the Reynolds stress tensor. This tensor introduces six new unknown variables, consequently the set of equations for the URANS model are not closed and further modeling is necessary. Among the options to express the Reynolds stress tensor in terms of known quantities, the most widely used methods correlates the mean velocity gradient and the Reynolds stress tensor. In this regard, the most popular approach is to use the Boussinesq hypothesis, which

prescribes a relation between the turbulent tensor and the kinematic eddy viscosity where the transfer of momentum by diffusion in molecular level is similar to the transfer of momentum in a turbulent flow due to the turbulent fluctuations. The Reynolds shear stresses tensor is given by

$$\bar{\mathbf{U}}' \bar{\mathbf{U}}' = \nu_t (\nabla \mathbf{U} + (\nabla \mathbf{U})^T) + \frac{2}{3} k \mathbf{I}, \quad (24)$$

where \mathbf{I} is the identity matrix, and k is the specific turbulent kinetic energy given by

$$k = \frac{1}{2} \bar{\mathbf{U}}' \cdot \bar{\mathbf{U}}'. \quad (25)$$

The evaluation of the kinematic eddy viscosity ν_t , can be made through different ways such as algebraic relations, or by solving transport equations. However, the most common method is to obtain the kinematic eddy viscosity as a function of the specific turbulent kinetic energy and its specific dissipation rate which stands out for the so called two-equations turbulent model [44]. Thus, the kinematic eddy viscosity and the specific dissipation rate are given by

$$\nu_t = C_\mu \frac{k^2}{\epsilon}, \quad (26)$$

$$\epsilon = \frac{1}{2} \nu_t \{ \nabla \bar{\mathbf{U}}' + (\nabla \bar{\mathbf{U}}')^T \} : \{ \nabla \bar{\mathbf{U}}' + (\nabla \bar{\mathbf{U}}')^T \}. \quad (27)$$

The CFD simulations conducted in this work were for turbulent flows, and amongst the variety of the two-equations models, the current investigations employed the $k-\omega$ SST turbulence model from [23], due its ability of predict flows with strong adverse pressure gradient with higher performance when compared to the variation of the $k-\omega$ models from [44], and the baseline (BSL) from [45]. Therefore, by considering this model, the governing equations incorporating the low-Reynolds corrections are presented as follows for the ϵ and ω relation, the specific turbulent kinetic energy k and the specific dissipation rate ω

$$\omega = \frac{\epsilon}{C_\mu k}, \quad (28)$$

$$\frac{\partial k}{\partial t} + \nabla \cdot (\mathbf{U} k) = \nabla \cdot [(\nu + \nu_t \sigma_k) \nabla k] + \tilde{P}_k - \beta^* k \omega, \quad (29)$$

$$\begin{aligned} \frac{\partial \omega}{\partial t} + \nabla \cdot (\mathbf{U} \omega) &= \nabla \cdot [(\nu + \nu_t \sigma_\omega) \nabla \omega] + \frac{\alpha}{\nu_t} \tilde{P}_k - \beta \omega^2 + \\ &2(1 - F_1) \frac{\sigma_{\omega^2}}{\omega} \nabla k \cdot \nabla \omega. \end{aligned} \quad (30)$$

Table 1: SST k- ω turbulence model auxiliary relations.

$v_t = \frac{k}{\omega} \cdot \min\left(\alpha^*, \frac{a_1 \omega}{S_2 F_2}\right)$
$S_t = \sqrt{\mathbf{S}_t \cdot \mathbf{S}_t}$
$\mathbf{S}_t = \frac{1}{2} [(\nabla \mathbf{U}) + (\nabla \mathbf{U})^T]$
$\alpha^* = \alpha_\infty^* \left(\frac{\alpha_0^* + Re_T/R_k}{1 + Re_T/R_k} \right)$
$D_\omega^+ = \max(2\rho\sigma_{\omega 2} \frac{1}{\omega} \nabla(k\omega), 10^{-10})$
$P_k = v_t \nabla \mathbf{U} [(\nabla \mathbf{U}) + (\nabla \mathbf{U})^T]$
$\tilde{P}_k = \min \cdot (P_k, 10\beta^* \rho k \omega)$
$\alpha = \frac{\alpha_\omega}{\alpha^*} \left(\frac{\alpha_0 + Re_T/R_\omega}{1 + Re_T/R_\omega} \right); Re_T = \frac{k}{v\omega}$
$F_1 = \tanh \left\{ \min \left[\max \left(\frac{\sqrt{k}}{\beta^* \omega d}, \frac{500 \nu}{d^2 \omega} \right), \frac{4\rho\sigma_{\omega 2} k}{D_\omega^+ d^2} \right] \right\}^4 \right\}$
$F_2 = \tanh \left\{ \left[\max \left(\frac{2\sqrt{k}}{\beta^* \omega d}, \frac{500 \nu}{d^2 \omega} \right) \right]^2 \right\}$

The last term on the right side of Eq. (30) denotes the cross-diffusion which represents the standard $k - \varepsilon$ into the means of the $k - \omega$, and C_μ is a constant equal to 0.09. The auxiliary relations of the $k-\omega$ SST model are presented in Table 1.

The specific kinetic energy production P_k is considered in the transport equations, Eqs. (29) and (30), and \tilde{P}_k is a production limiter to prevent the formation of turbulence in stagnation areas. In addition, we use the blending functions F_1 and F_2 defined by [23]: F_2 is equal to one in boundary layers and zero in free shear layers, and F_1 is blended with the model coefficients, which include σ_k , σ_ω , α_∞ , and β by the relation expressed in generic form by

$$\phi = \phi_1 F_1 + \phi_2 (1 - F_1), \quad (31)$$

where ϕ represents the coefficients σ_k , σ_ω , α_∞ , and β . Finally, to close all the model requirements, the constants values are presented in Tab. 2.

2.6. Near-wall region treatment

The features of the turbulence close to the wall are highly different from the other regions of the flow, thus an appropriated model to treat the near wall region is required. To estimate the turbulent flow close to the wall, a mesh refinement must be considered which must satisfy the requirement of the turbulence model based on the y^+ variable.

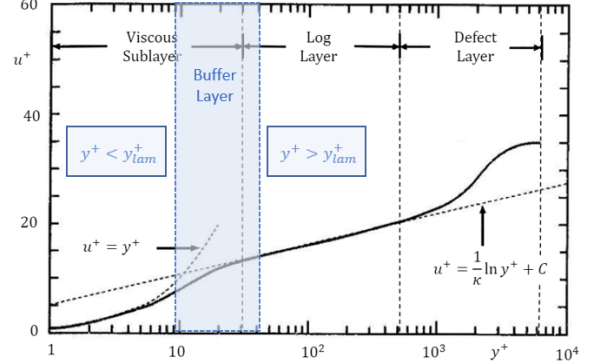


Figure 2: Velocity profiles and different regions of a turbulent boundary layer, edited from [44].

In the current investigations, k and ω were modeled by the low Reynolds wall functions representing a model which can switch between the viscous and logarithmic regions of the boundary layer according to the position of y^+ . In addition, v_t is obtained using the Spalding wall function model [46, 47], which also switch between viscous and logarithmic regions based on the value of y^+ . Fig. 2 illustrates the velocity profiles of the near wall regions.

In the OpenFOAM software, this method was implemented as explained in [48], by considering the y_{lam}^+ parameter as reference. The y_{lam}^+ is calculated to identify the region of the wall function by,

$$y_{lam}^+ = \frac{\log(\max(Ey^+, 1))}{\kappa},$$

where E is equal to 9.8 for smooth walls and κ is the von Kármán constant, equals to 0.41. The y^+ parameter is given by

$$y^+ = \frac{yu_\tau}{\nu}, \quad (32)$$

where u_τ is the friction velocity,

$$u_\tau = C_\mu^{1/4} \sqrt{k}, \quad (33)$$

and k is the value of kinetic energy of the cell center adjacent to the wall obtained through the relation $k = k^+ \times u_\tau^2$. If $y^+ > y_{lam}^+$, the kinetic energy is estimated as

$$k^+ = \frac{C_k}{\kappa} \log(y^+) + B_k,$$

where C_k and B_k are turbulence model constants equal to -0.416 and 8.366 respectively, and the dissipation rate is given by

$$\omega = \frac{k^{\frac{1}{2}}}{C_\mu^{1/4} \kappa y}. \quad (34)$$

Table 2: SST k - ω turbulence model constants.

$R_k = 6$	$R_\omega = 2.95$	$\alpha_0 = 1/9$	$a_0^* = 0.024$	$\sigma_{k,1} = 0.85$	$\sigma_{k,2} = 1.0$	$\alpha_{\infty,1} = 5/9$
$\alpha_{\infty,2} = 0.44$	$\sigma_{\omega,1} = 0.5$	$\sigma_{\omega,2} = 0.856$	$\beta_1 = 0.075$	$\beta_2 = 0.0828$	$\beta^* = 0.09$	$a_1 = 0.31$

If $y^+ < y_{lam}^+$, the kinetic energy and the dissipation rate are estimated as

$$k^+ = \frac{2400}{C_e^2 \times C_f} \quad (35)$$

and

$$\omega = \frac{6.0\nu}{\beta_1 y^2}, \quad (36)$$

where β_1 is a turbulence constant equals to 0.075. Finally, the eddy viscosity estimation is given by the following relations,

$$v_t = \frac{(u_\tau)^2}{\partial \mathbf{U}/\partial n} - v, \quad (37)$$

$$y^+ = u^+ + \frac{1}{E} \left[e^{\kappa u^+} - 1 - \kappa u^+ - \frac{1}{2} (\kappa u^+)^2 - \frac{1}{6} (\kappa u^+)^3 \right], \quad (38)$$

where if $y^+ > y_{lam}^+$,

$$u^+ = \frac{Ey^+}{\kappa}, \quad (39)$$

while if $y^+ < y_{lam}^+$,

$$u^+ = y^+. \quad (40)$$

3. Numerical Simulations

In this section we detail the setup and parameters of the numerical investigations of the performance of the NREL baseline 5 MW offshore wind turbine in full scale. The data analyzed includes the power production, blade loading and wake aerodynamics pattern. The full wind turbine geometry is composed by three blades, the hub, the tower, and the nacelle, and more details about the design are available in [19]. Fig. 3 illustrates the case being investigated, which consists of the 5 MW wind turbine placed on an offshore site under the influence of a logarithmic non-turbulent wind profile.

3.1. Computational Domain and Boundary Conditions

The full geometry was built using the software Solid Edge and imported into OpenFOAM, whereas all other parts of the computational domain were built around the wind turbine geometry using the snappyHexMesh

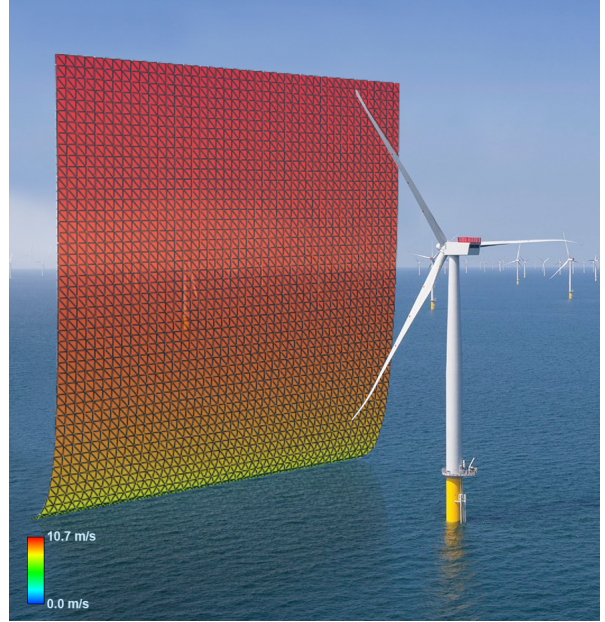


Figure 3: Visualization of the case being investigated, which includes a 5 MW offshore wind turbine in full scale operating under a logarithmic non-turbulent wind profile.

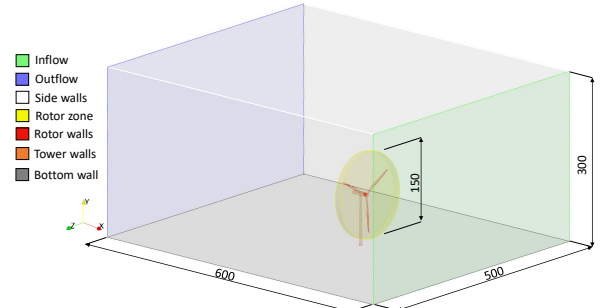


Figure 4: NREL baseline 5 MW offshore wind turbine computational domain dimensions (in meters) and boundary conditions.

utility. Fig. 4 illustrates the computational domain dimensions in meters and the boundary conditions, which were defined as in [49].

For all cases investigated the dimensions of the computational were the same: 500 m wide, 600 m long and 300 m high. The boundary conditions were also the same. At the inflow, the boundary condition for the velocity was of Dirichlet type, given by a prescribed logarithmic described as

$$U_x = v_o \frac{\log(y/z_o)}{\log(h_o/z_o)}, \quad (41)$$

where v_o is the velocity at 80 m high, chosen to be 10 m/s. Considering the location of the wind turbine in a offshore site, the roughness height z_o was set to be 0.001 m, representing the ocean rugosity. y represents the height variation and h_o is the reference height considered as 80 m (hub height). Still at the inflow, the boundary condition for the pressure was a null gradient (Neumann condition). For the turbulent quantities Dirichlet conditions were employed, with prescribed values estimated based on the most critical Reynolds number (at the blade tip), through the turbulence Reynolds number (Re_L) suggested by [50], used to estimate the turbulence length scale and the turbulence intensity. Based on that, the turbulence length scale for this region was 0.175 m, the turbulence kinetic energy $k = 3.2651 \text{ m}^2\text{s}^{-2}$, and the dissipation rate $\omega = 18.649 \text{ m}^2\text{s}^{-3}$, while the eddy viscosity was calculated based on the internal field everywhere. At the side and top planes, the boundary conditions for the velocity were symmetric plane condition, which corresponds to null normal velocity and zero normal gradient for the tangential velocity, pressure and turbulent quantities. For the turbine walls, no slip condition was imposed. At the rotor walls, the boundary condition for the velocity was of Dirichlet type. Since the mesh around this region is dynamic, a uniform rotor velocity of 1.1649 rad/s was prescribed, which is the rotor speed for a wind speed of 10 m/s. On the rotor walls and tower walls, Neumann boundary condition is applied for the pressure as a null gradient, while the turbulence properties receive the proper wall function treatment according with the y^+ value in the near wall region. At the outflow, the pressure was set to zero and the boundary condition for all other flow variables was null gradient.

3.2. Spatial discretization

To perform the simulations, two different meshes, Mesh-1 and Mesh-2, were built considering different refinement strategies. Both meshes were built considering the same computational domain presented in Fig. 4.

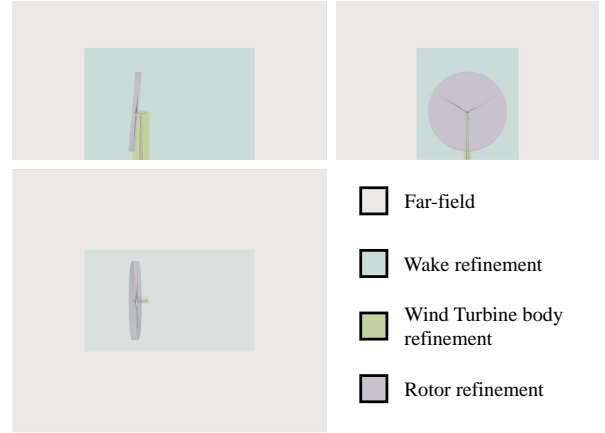


Figure 5: Strategical partition of the computational domain to apply different mesh refinements.

To build the non-uniform unstructured meshes, first the computational domain was decomposed in four main regions as presented in Fig. 5. Even though the partition of the computational domain regions was the same between the meshes being investigated, different cell sizes were adopted for each mesh. Table 3 presents the refinement applied in each region of the computational domain for both meshes being investigated. Regarding the mesh communication between the static and dynamic parts of the mesh, an arbitrary mesh interface (AMI) methodology [51] was considered for both meshes.

The main difference between the refinement strategies is in the rotor region where the cells size was increased from 0.5 m for Mesh-1 to 1 m for Mesh-2, and in the wake region, where the cells size was increased from 1.5 m for Mesh-1 to 2 m for Mesh-2. Different cell sizes were adopted in the far field for both meshes, for Mesh-1 it started with element size of 25 m and decreased to 0.75 m close to the wind turbine. On the other hand, for Mesh-2 it started with element size of 8 m and decreased to 1 m close to the wind turbine. As a result, Mesh-1 and Mesh-2 were composed by 19,942,667 and 20,744,243 cells respectively. More details about the refinement strategy applied in each partition of the computational domain considered for each mesh being investigated can be seen in Fig. 6.

In addition, to perform the blade-resolved investigations considering the tower influence, a proper refinement close to the edges of the blades and tower, which must preserve the variation of the y^+ parameter in all these regions, is required. Fig. 7 illustrates the details of the meshes at different positions along the blade span indicated by R , and different distance from the ground indicated by H , when the blade is at azimuth angle of 180°

Table 3: Mesh sizing information (in meters) for each region of the computational domain for Mesh-1 and Mesh-2.

Region	Mesh-1	Mesh-2
Fafield	25	8
Wake refinement	1.5	2
WT body refinement	0.75	1
WT body surface	0.18	0.25
WT first cell height	0.01	0.01
Growth rate	1.332	1.332
Nº Layers	10	10
Rotor refinement	0.5	1
Blade region	0.0625	0.0625
Blade surface	0.0625	0.0625
Blade first cell height	0.001	0.001
Growth rate	1.38	1.38
Nº Layers	10	10
Total cells number	19,942,667	20,744,243

which is in front of the tower. The information about the discretization properties at the different regions of the blade and tower is presented in Tab. 4, which includes the first cell height adopted in order to achieve the y^+ desired.

3.3. Numerical schemes

In all simulations the divergence terms were discretized using a second-order upwind scheme, chosen based on the modeling of similar problems to compute the convective fluxes [10, 31]. Central differences were employed for the Laplacian terms, and the least-squares cell-based scheme was adopted for the gradient terms. The set of linear equations was solved using the geometric-algebraic multi-grid (GAMG) algorithm for the symmetric matrices, and the preconditioned bi-conjugate gradient (PBiCG) with the DILU preconditioner for the non-symmetric matrices, as suggested by [43].

About the temporal discretization, as aforementioned, the second order implicit backward scheme was employed. The CFL number was limited and controlled by an adaptive time step to guarantee stability during the iterative process. Different CFL numbers were considered for Mesh-2 in order to understand the sensitivity of the accuracy of the results and computational cost with respect to this parameter. This was possible because the CFL number can be larger than 1 for implicit schemes, since they are less sensitive to a numerical instabilities [36].

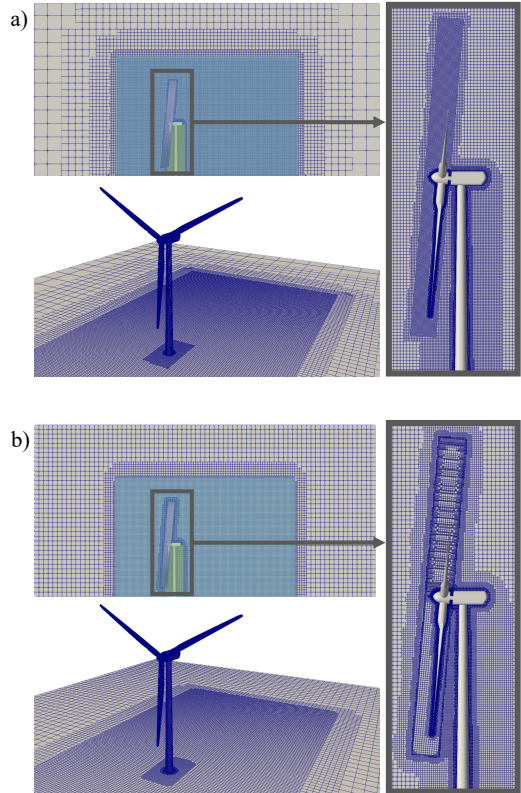


Figure 6: Spatial discretization of the computational domain regions considered for a) Mesh-1, and b) Mesh-2.

3.4. Solver information

For Mesh-1, two different iterative PISO algorithms were implemented, as presented in Fig. 1, which includes the iterative PISO in its generic form and the iterative PISO with flux correction. For both investigations the pressure-based solver considered 5 sub-iterations for each time step and 2 corrections for pressure. The CFL number was limited to 2 for the transient analyses in both cases. For Mesh-2, only the iterative PISO with flux correction was considered.

The URANS $k - \omega$ SST turbulence model was employed in all cases and the iterations were considered converged when the residuals of the set of estimated variables was equal or less than 10^{-6} . For each mesh, the initial conditions for the transient problem for all properties were the steady state solution for the problem after 500 iterations, obtained with the steady form of the SIMPLE algorithm. The computations were carried out in the Brazilian supercomputer Santos Dumont. To run the simulations the meshes were partitioned into 240 sub-domains using scotch decomposition, allocating 10 nodes in the cluster, where each node had two 12

Table 4: Spatial discretization information at different positions along the blade span, indicated by R, and different distance from the ground, indicated by H, for Mesh-1 and Mesh-2

	Blade	Tower	Blade	Tower	Blade	Tower
Position (Azimuth = 180°)	R = 20 m	H = 70 m	R = 40 m	H = 50 m	R = 60 m	H = 30 m
First cell height	1×10^{-3} m	1×10^{-2} m	1×10^{-3} m	1×10^{-2} m	1×10^{-3} m	1×10^{-2} m
Characteristic length	Chord	Diameter	Chord	Diameter	Chord	Diameter
	4.65 m	4.3 m	3.63 m	4.79 m	1.2 m	5.27 m
Re_{local}	7.2×10^6	2.8×10^6	11.3×10^6	3.1×10^6	11.7×10^6	3.3×10^6
Local air speed	23.2 m/s	9.9 m/s	46.6 m/s	9.65 m/s	69.9 m/s	9.28 m/s
y^+	60	260	120	253	180	242

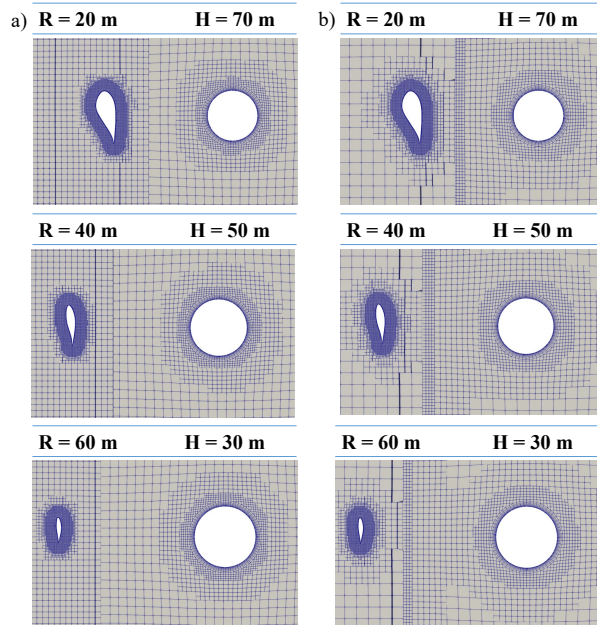


Figure 7: Spatial discretization at different positions along the blade span, indicated by R and different distances from the ground, indicated by H, for a) Mesh-1 and b) Mesh-2.

core Intel Xeon Cascade Lake Gold 6252 processors, 3.7 GHz, and 256 Gb of RAM.

4. Results and discussion

First the results obtained with Mesh-1 regarding the different approaches of the iterative PISO solver as presented in Fig. 1 are presented. Next, a comparison between the different meshes using the same numerical setup is made to choose the more suitable one when comparing the computational cost and the accuracy of the results. Finally, Mesh-2 is used for an investigation about the temporal discretization.

4.1. Iterative PISO solver approaches

Here we compare the two different approaches of the iterative PISO solver, presented in Fig. 1, and the results are presented in two parts. First, comparisons of the generated thrust, power production and the forces distribution along the blade span obtained with both setups are presented, along with the results from the NREL OpenFAST code [42], considering the same environmental conditions. Subsequently, a discussion is made based on the computational cost associated with each approach of the iterative PISO solver tested.

4.1.1. Verification with OpenFAST

OpenFAST v2.5.0 [42] is a code capable of analyzing three-bladed horizontal-axis wind turbines including the tower influence considering the offshore environmental conditions in the time domain. It uses the blade element momentum theory and tip corrections to calculate the aerodynamic loads on the blades.

Fig. 8 illustrates a comparison of the wind turbine power production and the generated thrust for both algorithms of the iterative PISO tested, the generic form, and with an extra correction for pressure due to the face flux correction applied before the start of the solver loop. Besides, both CFD simulations results are benchmarked against the OpenFAST results.

Looking at the generated power and thrust comparison between the two approaches of the iterative PISO solver, Fig. 8, it is possible to notice that the generic form of the solver presented very similar results in terms of low frequency components when compared to the approach with face flux correction, which can also be attested by looking at mean values in Tab. 5, for both power production and thrust. However, the time series presented significant noise for the generic form of the iterative PISO solver while for the approach with the extra pressure correction this behaviour was not observed. Since the wind profile considered in the investi-

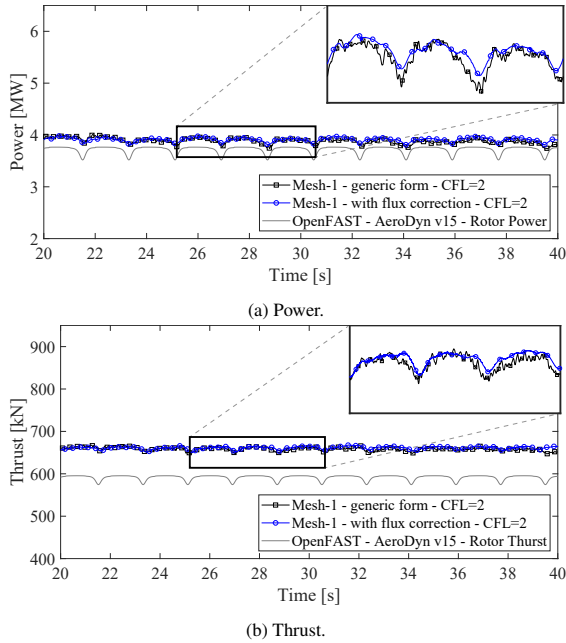


Figure 8: Generated power and thrust comparison between the iterative PISO solver using the generic form and with flux correction approaches, benchmarked against OpenFAST results.

gation is non-turbulent, the instabilities captured in the generic form sign is interpreted as an oscillation caused by the numerical arrangement. Both algorithms presented higher mean values for both generated power and thrust when compared with OpenFAST results.

In addition, the distribution of the mean forces along the blades were also investigated and compared. As presented in Fig. 9, both methodologies of the iterative PISO solver presented similar behaviour in the normal and tangential forces prediction along the blade span, for both positions of the blade being analyzed. The 0° azimuth angle represents the blade aligned with the

Table 5: NREL 5 MW wind turbine performance comparison between the CFD simulations and OpenFAST code results.

	Mean	
	Power [MW]	Thrust [kN]
Mesh-1: generic CFL 2	3.88 ± 0.05	658.5 ± 4.4
Mesh-1: F corr. CFL 2	3.91 ± 0.04	664.4 ± 3.0
Mesh-2: F corr. CFL 1	3.49 ± 0.06	636.6 ± 5.5
Mesh-2: F corr. CFL 2	3.84 ± 0.05	636.6 ± 3.6
Mesh-2: F corr. CFL 4	4.08 ± 0.05	685.2 ± 3.4
OpenFast AeroDyn	3.72 ± 0.07	591.4 ± 5.9

wind turbine in the z -direction pointing to the top wall of the computational domain, while the 180° azimuth angle represents the blade aligned with the wind turbine in the z -direction pointing to the bottom wall of the computational domain, which represents the position of the blade when it is crossing in front of the tower.

A computational cost analysis considering the performance of each of the tested approaches showed that the extra face flux correction can be performed without significant extra computational demand as shown in Fig. 10. Both methodologies took approximated 11 hours to complete the simulation of one second. The variation between the time to calculate one time step was on average 14.97 s for the generic form of the iterative PISO solver, against 15.61 s for the approach considering the face flux correction.

Therefore, considering the computational cost and numerical accuracy, we concluded that the most suitable solver option was the iterative form of the PISO algorithm with the face flux correction. The numerical behaviour of the time series signs are important in such analysis while the turbulent wind which is one of the next steps to be considered in our work.

4.2. Investigation of spatial discretization strategies considering the iterative PISO solver with face flux correction

As presented in Figs. 6 and 7, different spatial discretization strategies were considered for the Mesh-1 and Mesh-2. The results are presented in three parts. First a comparison of the generated thrust, power production and forces distribution along the blade span obtained with the different meshes are presented along with the results obtained with OpenFAST considering the same environmental conditions as performed in the CFD simulations. In sequence, the visualization of the flow features for each mesh is shown. Finally, a discussion is made based on the computational cost associated with each test run.

4.2.1. Verification with OpenFAST

A comparison for the wind turbine power production and generated thrust obtained through the CFD simulations, considering both spatial discretization strategies, and the results obtained with OpenFAST considering the same environmental conditions are shown in Fig. 11. It is possible to notice that both meshes presented similar results, slightly higher than those from OpenFAST. This can also be seen in Tab. 5. However, the results obtained with Mesh-2 were closer to those from OpenFAST.

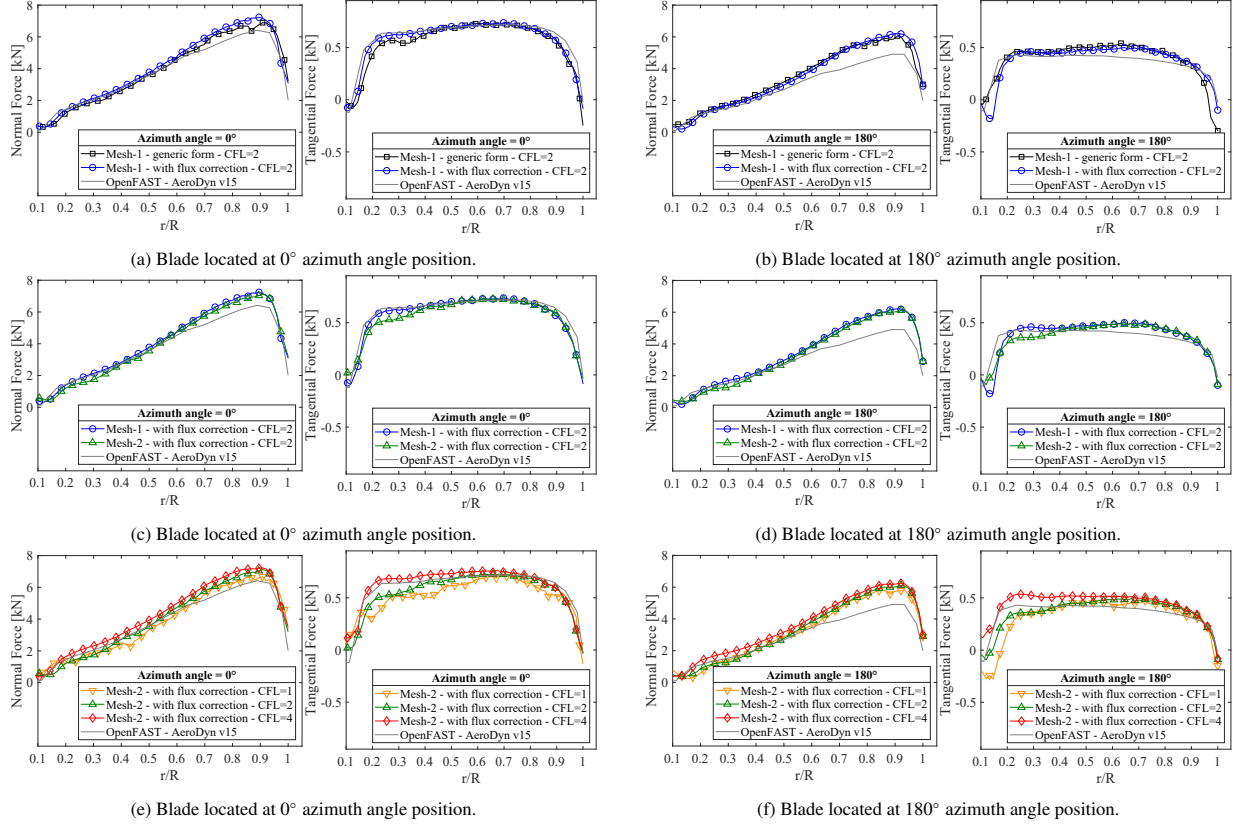


Figure 9: NREL 5 MW wind turbine comparison of the distributed forces along the blade span for all the CFD simulations benchmarked against the OpenFAST results considering the same environmental conditions.

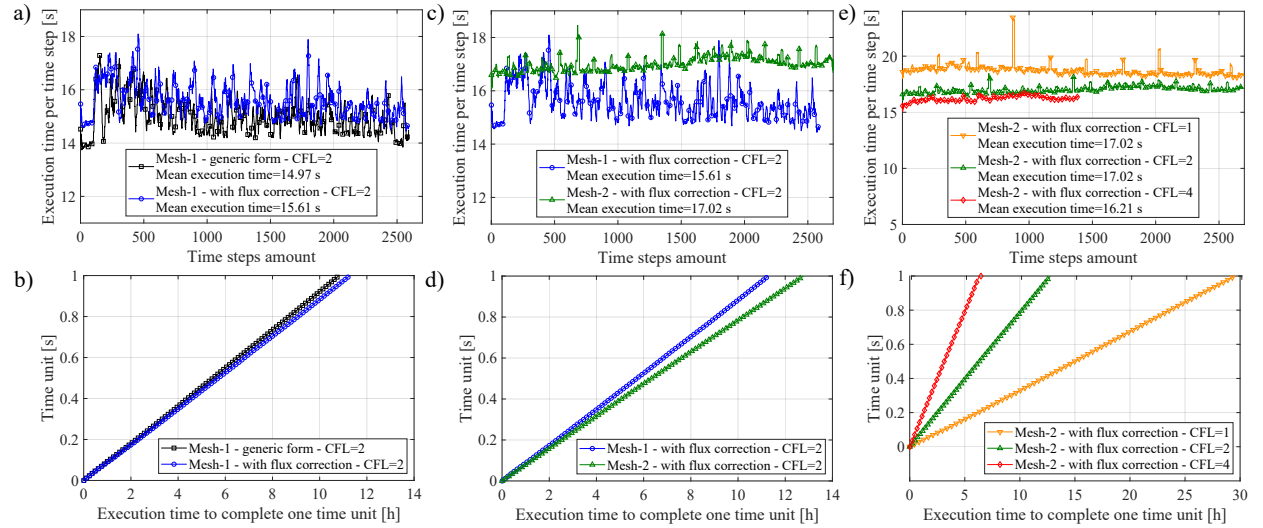


Figure 10: Computational cost comparison for all the CFD simulations presented in Section 4.

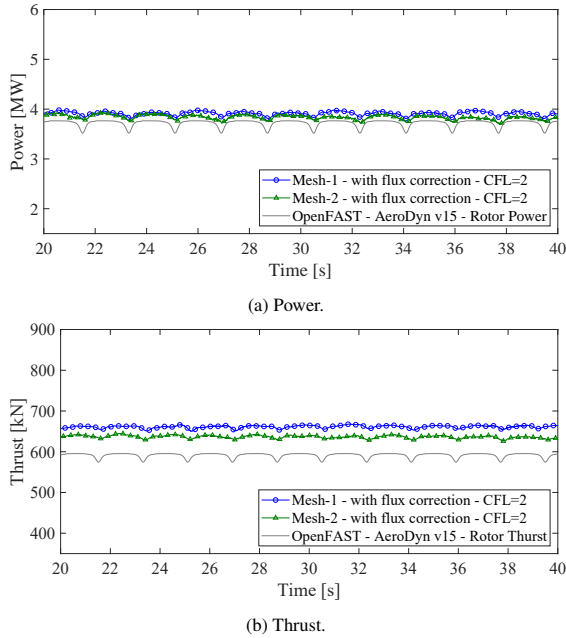


Figure 11: Generated power and thrust comparison between the Mesh-1 and Mesh-2 using the iterative PISO solver with flux correction benchmarked against OpenFAST results.

It is also clear that power production results were very close to each other, while the generated thrust exhibited more noticeable differences. The force distributions in Fig. 9 c) and d) provide further insight into this result. We can see that the differences in the normal force are more significant than those in the tangential force, so this is consistent with seeing larger differences in thrust than in power. For both forces, the differences are higher close to the tip of the blade, and this can be related to the three-dimensional character of the flow in that region. It is important to remember that OpenFAST employs BEM to calculate the forces, which is an essentially two-dimensional method, with tip correction factors to account for some of the three-dimensional effects [52]. One of the BEM assumptions is that there is very little spanwise pressure variation, and the theory is therefore less accurate for heavily loaded rotors with large pressure gradients across the span. Furthermore, higher differences are seen at 180° azimuth angle position, when compared to 0° . At 180° , the blade is right in front of the tower so the proximity with that structure alters the flow significantly. In OpenFAST, this effect is accounted for considering a potential flow approximation for the field around the tower, but this is certainly not very accurate for this complex flow. In addition, the tip and hub vortex, which are also overlooked in Open-

FAST, influence the induced velocities and generates a skewed flow which impacts significantly in the prediction of the wind turbine thrust.

4.2.2. Flow structures

Contours of the axial velocity on a vertical plane, considering the tower influence with the blade located in front of the tower, are presented in Fig. 12 for both meshes investigated. This figure shows that both meshes predicted the wake pattern taking into account perturbations which affect the wake structure as consequence of the influence of the tower, hub-nacelle and blade tip vortices. However, different resolutions in the wake can be observed. For Mesh-1, the velocity field in the center of the wake presents stronger gradients when compared to the results from Mesh-2.

The primary component of the wake behaviour is captured through the vortex information represented by the second invariant of the velocity gradient tensor, the Q-criterion ($Q = 0.05$), illustrated in Fig. 13. In that figure, we can see different patterns for each mesh being investigated. For Mesh-2 the vortical structures along the blade span are mitigated, whereas Mesh-1 captures better the disturbances which are related with the spanwise flow. These differences between the results for each mesh is due to the resolution of the mesh in the rotor region, which is higher for Mesh-1. However, even though in Mesh-2 this flow features are damped, the wake intensity remains with a similar behaviour and the prediction of the wind turbine performance results were slightly closer to those from OpenFAST.

More details of the blade-tower interaction for both meshes are illustrated in Fig. 14 through the instantaneous axial velocity and normal vorticity contours at different positions along the blade span, indicated by R, and above the ground, indicated by H. By comparing the results for Mesh-1 and Mesh-2, it is possible to observe different behaviour of the vortex pattern shed by the tower in the three regions analyzed, while for the rotor blades the behaviour is similar. In addition, some differences can be noticed in the wake pattern when the normal vorticity contours are compared, such as the wake contour which was more stable for the Mesh-2.

The computational cost presented in Fig. 10 c) and d) shows that, even though the time to complete one second of the simulation time is around 12 hours for both meshes, Mesh-1 presented a slight improvement in the time to calculate one time-step, which was 15.61 s, while for Mesh-2 it was 17.02 s. The most suitable option is here considered as Mesh-2 due to the increase in the results accuracy at an acceptable computational demand.

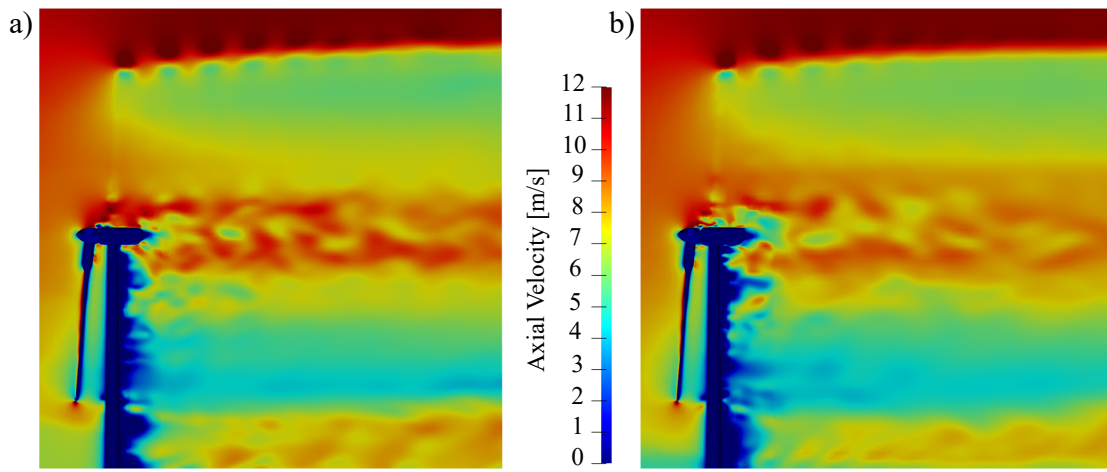


Figure 12: NREL 5 MW wind turbine results comparison of the instantaneous iso-contours of the axial velocity for a) Mesh-1 and b) Mesh-2.

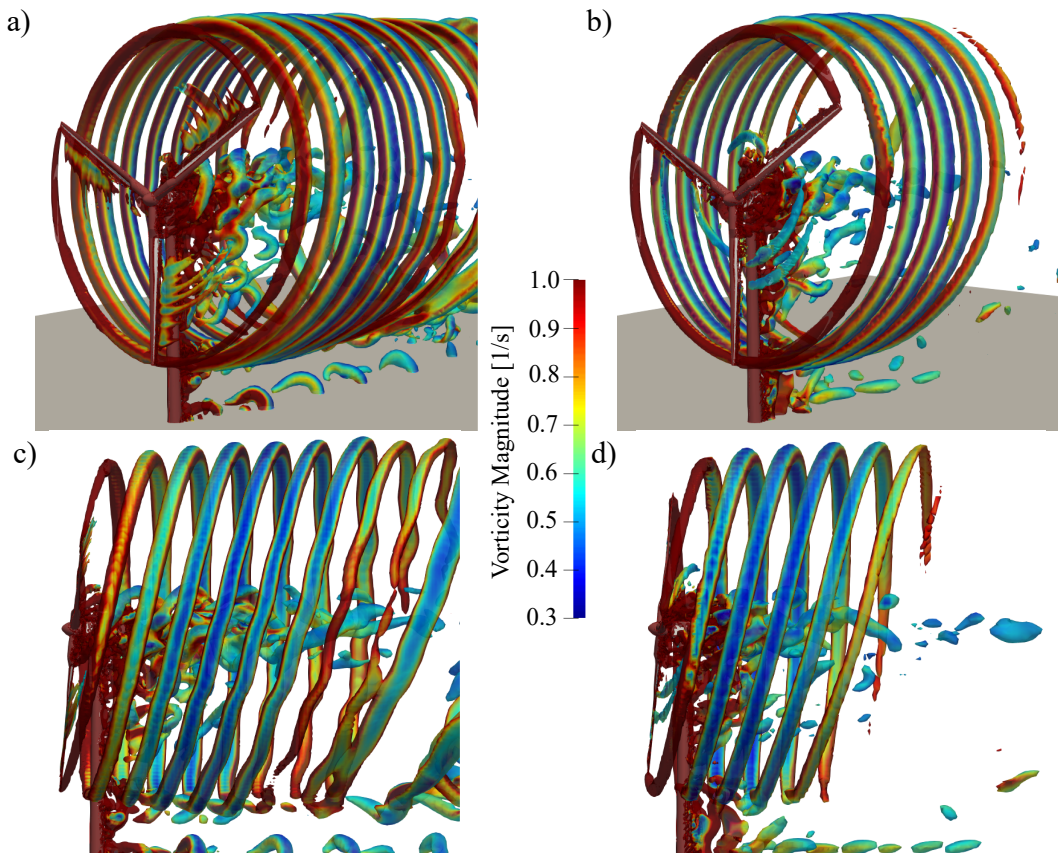


Figure 13: NREL 5 MW wind turbine results comparison of the instantaneous isosurfaces of the Q-criterion ($Q=0.05$) colored by vorticity magnitude shown in perspective and side view for Mesh-1 a) and c) and for Mesh-2 b) and d) respectively.

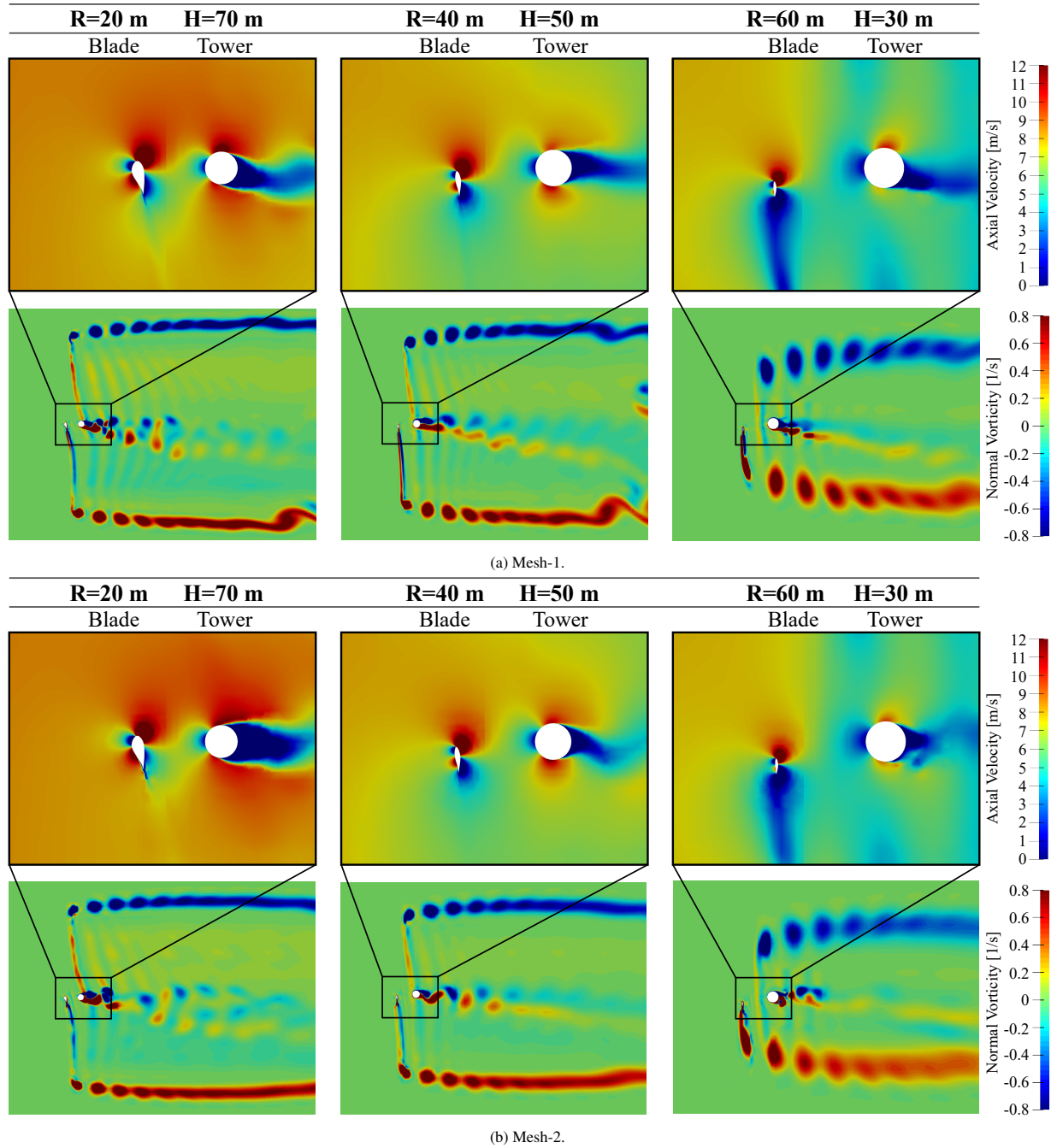


Figure 14: NREL 5 MW wind turbine results comparison of the instantaneous iso-contours of the axial velocity and normal vorticity in different positions along the blade span indicated by R and above the ground indicated by H, for a) Mesh-1 and b) Mesh-2.

4.3. Temporal discretization investigation for Mesh-2 and iterative PISO with face flux correction

A temporal discretization analysis, which is strongly recommended in the modeling of transient problems, is performed in this section considering different CFL numbers for Mesh-2. Like in the previous analyses, the results are presented in three parts. First a comparison of performance results in terms of generated thrust, power production and forces distribution along the blade span are presented along the results obtained with OpenFAST, for the same environmental conditions as performed in the CFD simulations. We also analyse the computational cost associated with each case being investigated. Next, a comparison of the flow features for each CFL is presented.

4.3.1. Verification with OpenFAST

A comparison for the wind turbine power production and generated thrust obtained through the CFD simulations, considering all CFL numbers investigated, and the results obtained with OpenFAST, considering the same environmental conditions, are illustrated in Fig. 15. It is possible to notice that with the increase in the CFL number the accuracy in the results prediction is reduced since the differences between the expected values obtained with OpenFAST and the CFD simulation are considerably increased for both power and thrust (see also the mean values as presented in Tab. 5). This behaviour is here considered to be a consequence of an unappropriated time step sizing which is increased for higher CFL numbers. The size of the time step is related to the temporal scales that can be captured in the simulations. By increasing the CFL number, the use of a larger time step filtered out some important characteristics of the flow which resulted in loss of accuracy in the results.

Figures 9 e) and f) show the distribution of the tangential and normal forces along the blades span. These results also vary significantly when the CFL number is increased. When the CFL number was equal to 4, we observed a higher tangential force in the regions close to the blade root for both blade positions.

The computational cost results presented in Fig. 10 e) and f) show that the increase in the CFL number reduces the computational demand. From CFL number of 2 to 4 the time to execute one second of the simulation time was reduced from 12 hours to 6 hours, due to the reduction in the amount of time steps required to execute the same simulation time. However, the loss of accuracy is significant and the CFL number of 4 is not a suitable option. Following with this analyses, the most suitable option for the temporal discretization is

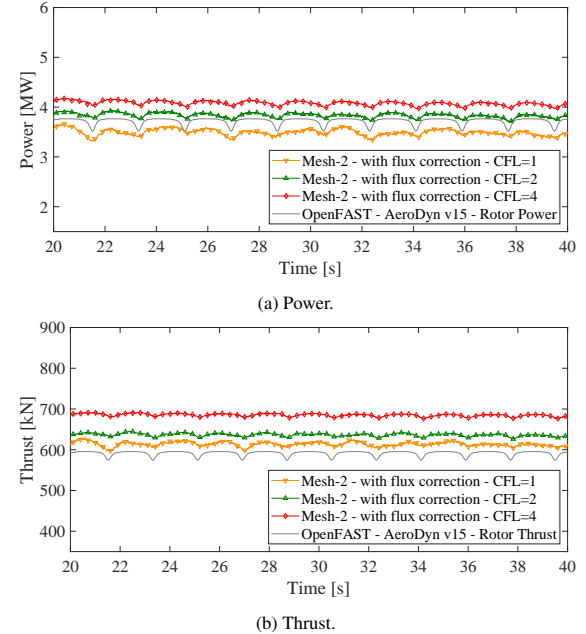


Figure 15: Generated power and thrust comparison between different CFL numbers considered for Mesh-2 using the iterative PISO solver with flux correction benchmarked against OpenFAST results.

here considered as the CFL number equal to 2 due to the acceptable results accuracy and less computational demand when compared with CFL number equal to 1.

4.3.2. Flow structures

In Figs. 16 a), b) and c), it is possible to notice through the instantaneous axial velocity contours, that the increase in the CFL number changes the gradient of axial velocity significantly in the wake region. With CFL number equals to 4, the reduction in the axial velocity caused by the blades is higher, which resulted in the over estimation of the wind turbine power, thrust, and the forces distributions along the blade span close to the blade root. Looking at the instantaneous iso-surfaces of the Q-criterion ($Q = 0.05$) colored by the vorticity magnitude, Figs. 16 d), e) and f), it is clearly observed that with the increase in the CFL number, less vortical structures are captured. As a consequence, differences in the axial velocity gradient from the blade-tower interaction and vortex shedding pattern are also noticed in Figs. 16 g) to l), respectively.

Therefore, by considering the temporal discretization investigation employed in the analyses of the NREL 5 MW wind turbine, the accuracy in the performance results were better predicted by the numerical model considering the CFL numbers 1 and 2. However, since the

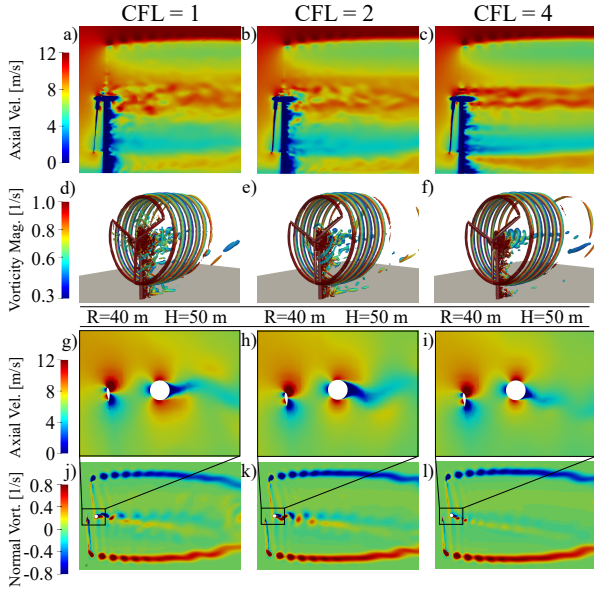


Figure 16: Comparison of the flow characteristics for Mesh-2 considering different CFL numbers given by a), b) and c) instantaneous axial velocitycontours. d), e) and f) instantaneous iso-surfaces of the Q-criterion ($Q = 0.05$) colored by the vorticity magnitude. g), h) and i) instantaneous axial velocity contours and j), k) and l) instantaneous normal vorticity contours, at 40 m of blade span and 50 m from the ground.

differences between the results are not large, when comparing the computational cost for both cases, we consider the most suitable option to conduct future investigations to be the spatial discretization given by Mesh-2 considering a temporal discretization limited by the CFL number equals to 2, and employing the iterative PISO with face flux correction as solver.

5. Conclusions

In this paper, a numerical investigation of the operation of the NREL 5 MW offshore wind turbine in full scale considering different approaches of the iterative PISO solver has been carried out. An extra correction for pressure considered through the inclusion of the face flux correction in the algorithm steps presented a more stable numerical behavior in relation to the convergence of the time series signals for the generated power and thrust. Since the wind profile considered in the investigation was non-turbulent, the instabilities captured by the generic form were attributed to numerical oscillations caused by the solver numerical arrangement. Therefore, as the approach with face flux correction can be performed without significant extra computational demand, this solver algorithm was chosen for

conducting the spatial and temporal discretization investigations.

By considering the iterative PISO algorithm with face flux correction as pressure-based solver, a spatial discretization investigation was performed by considering different refinement strategies. The performance results in terms of power production, generated thrust and forces distribution along the blade span were obtained for both meshes being investigated. In addition, a detailed comparison of the results in terms of visualization of the flow characteristics for both meshes was also performed, and by considering the computational cost Mesh-2 was chosen for conducting the analysis of the temporal discretization by considering different CFL numbers to limit the time step sizing.

Considering the Mesh-2 the present work allowed a better interpretation of the influence of the CFL number as a convergence parameter and its influence in the results accuracy for transient analyses. The increase in the CFL number presented a limitation due to the time step which became unappropriate to capture the flow temporal scales which represents the physics of the problem being investigated. CFL numbers close to the unit such as 1 and 2 presented satisfactory results, but the CFL equals to 1 requires higher computational demand than equals to 2.

5.1. Future work

Future work should employ the conclusions presented in this paper in the modeling of the next generation of larger wind turbines, such as IEA 15 MW [53], and the numerical investigations of FOWTs, like the NREL 5 MW mounted on an OC4 platform [54]. We believe that a complete CFD model, capable to predict the dynamic response of a FOWT under aerodynamic and hydrodynamic loads will be very useful to improve the understanding of this type of system, which will certainly become ubiquitous in the next few years.

Acknowledgments

M. de Oliveira acknowledges FAPESP (Fundação de Amparo à Pesquisa do Estado de São Paulo), the São Paulo Research Foundation, for the PhD grant - Process number 2018/26207-4. R. C. Puraca acknowledges FUSP/Petrobras for the PhD grant Project number 2019/00171-6. B. S. Carmo acknowledges the support from FAPESP, Proc. 2019/01507-8, for this research, and thanks the Brazilian National Council for Scientific and Technological Development (CNPq) for financial support in the form of a productivity grant, number 312951/2018-3. The authors also acknowledge the

grant from the National Laboratory of Scientific Computing (LNCC), CADASE project, which allowed the use of the Santos Dumont supercomputer to run the simulations that generated the results reported in this paper. This work is part of the European Commission Project “High Performance Computing for Wind Energy (HPCWE)” with agreement no. 828799.

References

- [1] H. Lund, Renewable energy strategies for sustainable development, *Energy* 32 (2007) 912–919.
- [2] G. W. E. Council, Gwec— global wind report 2021, Global Wind Energy Council: Brussels, Belgium (2017).
- [3] W. Ostachowicz, M. McGugan, J.-U. Schröder-Hinrichs, M. Luczak, MARE-WINT: new materials and reliability in offshore wind turbine technology, Springer Nature, 2016.
- [4] M. Karimirad, Offshore energy structures: for wind power, wave energy and hybrid marine platforms, Springer, 2014.
- [5] M. M. Hand, D. A. Simms, L. J. Fingersh, D. W. Jager, J. R. Cotrell, Unsteady Aerodynamics Experiment Phase V: Test Configuration and Available Data Campaigns, Technical Report, NREL, 2001. URL: <https://www.osti.gov/biblio/787980>. doi:10.2172/787980.
- [6] M. M. Hand, D. A. Simms, L. J. Fingersh, D. W. Jager, J. R. Cotrell, S. Schreck, S. M. Larwood, Unsteady Aerodynamics Experiment Phase VI: Wind Tunnel Test Configurations and Available Data Campaigns, Technical Report, NREL, 2001. URL: <https://www.osti.gov/biblio/15000240>. doi:10.2172/15000240.
- [7] L. Hayes, M. Stocks, A. Blakers, Accurate long-term power generation model for offshore wind farms in europe using era5 reanalysis, *Energy* 229 (2021) 120603.
- [8] Y. Zhang, S. Deng, X. Wang, Rans and ddes simulations of a horizontal-axis wind turbine under stalled flow condition using openfoam, *Energy* 167 (2019) 1155–1163.
- [9] B. Sanderse, S. Van der Pijl, B. Koren, Review of computational fluid dynamics for wind turbine wake aerodynamics, *Wind energy* 14 (2011) 799–819.
- [10] J. Thé, H. Yu, A critical review on the simulations of wind turbine aerodynamics focusing on hybrid rans-les methods, *Energy* 138 (2017) 257–289.
- [11] N. Sorensen, M. Hansen, Rotor performance predictions using a navier-stokes method, in: 1998 ASME Wind Energy Symposium, 1998, p. 25.
- [12] E. Duque, C. Van Dam, S. Hughes, Navier-stokes simulations of the nrel combined experiment phase ii rotor, in: 37th Aerospace Sciences Meeting and Exhibit, 1999, p. 37.
- [13] E. P. Duque, M. D. Burklund, W. Johnson, Navier-stokes and comprehensive analysis performance predictions of the nrel phase vi experiment, *J. Sol. Energy Eng.* 125 (2003) 457–467.
- [14] S. H. Park, J. H. Kwon, Implementation of kw turbulence models in an implicit multigrid method, *AIAA journal* 42 (2004) 1348–1357.
- [15] P. C. Rocha, H. B. Rocha, F. M. Carneiro, M. V. da Silva, A. V. Bueno, $k-\omega$ sst (shear stress transport) turbulence model calibration: A case study on a small scale horizontal axis wind turbine, *Energy* 65 (2014) 412–418.
- [16] M. J. Lawson, J. Melvin, S. Ananthan, K. M. Gruchalla, J. S. Rood, M. A. Sprague, Blade-Resolved, Single-Turbine Simulations Under Atmospheric Flow, Technical Report, National Renewable Energy Lab.(NREL), Golden, CO (United States), 2019.
- [17] P. Weihing, J. Letzgus, G. Bangga, T. Lutz, E. Krämer, Hybrid rans/les capabilities of the flow solver flower—application to flow around wind turbines, in: Symposium on hybrid RANS-LES methods, Springer, 2016, pp. 369–380.
- [18] Y. Zhang, A. van Zuijlen, G. van Bussel, Massively separated turbulent flow simulation around non-rotating mexico blade by means of rans and ddes approaches in openfoam, in: 33rd AIAA Applied Aerodynamics Conference, 2015, p. 2716.
- [19] J. Jonkman, S. Butterfield, W. Musial, G. Scott, Definition of a 5-MW reference wind turbine for offshore system development, Technical Report, National Renewable Energy Lab.(NREL), Golden, CO (United States), 2009.
- [20] R.-K. Zhang, V. D. J.-Z. Wu, Aerodynamic characteristics of wind turbine blades with a sinusoidal leading edge, *Wind Energy* 15 (2012) 407–424.
- [21] A. El Kasmi, C. Masson, An extended $k-\epsilon$ model for turbulent flow through horizontal-axis wind turbines, *Journal of Wind Engineering and Industrial Aerodynamics* 96 (2008) 103–122.
- [22] N. Tachos, A. Filios, D. Margaris, A comparative numerical study of four turbulence models for the prediction of horizontal axis wind turbine flow, *Proceedings of the Institution of Mechanical Engineers, Part C: Journal of Mechanical Engineering Science* 224 (2010) 1973–1979.
- [23] F. R. Menter, Two-equation eddy-viscosity turbulence models for engineering applications, *AIAA journal* 32 (1994) 1598–1605.
- [24] N. N. Sørensen, A. Bechmann, P.-E. Réthoré, F. Zahle, Near wake reynolds-averaged navier–stokes predictions of the wake behind the mexico rotor in axial and yawed flow conditions, *Wind Energy* 17 (2014) 75–86.
- [25] M. Moshfeghi, Y. J. Song, Y. H. Xie, Effects of near-wall grid spacing on sst- $k-\omega$ model using nrel phase vi horizontal axis wind turbine, *Journal of Wind Engineering and Industrial Aerodynamics* 107 (2012) 94–105.
- [26] M. O. L. Hansen, J. N. Sørensen, S. Voutsinas, N. Sørensen, H. A. Madsen, State of the art in wind turbine aerodynamics and aerelasticity, *Progress in aerospace sciences* 42 (2006) 285–330.
- [27] B. Latimer, A. Pollard, Comparison of pressure-velocity coupling solution algorithms, *Numerical Heat Transfer* 8 (1985) 635–652.
- [28] S. V. Patankar, Numerical heat transfer and fluid flow, CRC press, 2018.
- [29] R. I. Issa, Solution of the implicitly discretised fluid flow equations by operator-splitting, *Journal of computational physics* 62 (1986) 40–65.
- [30] S. V. Patankar, D. B. Spalding, A calculation procedure for heat, mass and momentum transfer in three-dimensional parabolic flows, in: Numerical prediction of flow, heat transfer, turbulence and combustion, Elsevier, 1983, pp. 54–73.
- [31] F. Bertagnolio, N. N. Sørensen, F. Rasmussen, New insight into the flow around a wind turbine airfoil section, *J. Sol. Energy Eng.* 127 (2005) 214–222.
- [32] E. Robertson, V. Choudhury, S. Bhushan, D. K. Walters, Validation of openfoam numerical methods and turbulence models for incompressible bluff body flows, *Computers & Fluids* 123 (2015) 122–145.
- [33] P. Cheng, Y. Huang, D. Wan, A numerical model for fully coupled aero-hydrodynamic analysis of floating offshore wind turbine, *Ocean Engineering* 173 (2019) 183–196.
- [34] H. K. Versteeg, W. Malalasekera, An introduction to computational fluid dynamics: the finite volume method, Pearson education, 2007.
- [35] H. Jasak, Dynamic mesh handling in openfoam, in: 47th AIAA aerospace sciences meeting including the new horizons forum

- and aerospace exposition, 2009, p. 341.
- [36] H. Jasak, Error analysis and estimation for the finite volume method with applications to fluid flows., Ph.D. thesis, Imperial College London (University of London), 1996.
- [37] B. Dose, H. Rahimi, B. Stoevesandt, J. Peinke, Fluid-structure coupled investigations of the nrel 5 mw wind turbine for two downwind configurations, *Renewable Energy* 146 (2020) 1113–1123.
- [38] Y. Liu, A CFD study of fluid-structure interaction problems for floating offshore wind turbines, Ph.D. thesis, University of Strathclyde, 2018.
- [39] W. Shi, J. Jiang, K. Sun, Q. Ju, Aerodynamic performance of semi-submersible floating wind turbine under pitch motion, *Sustainable Energy Technologies and Assessments* 48 (2021) 101556.
- [40] T. T. Tran, D.-H. Kim, A cfd study of coupled aerodynamic-hydrodynamic loads on a semisubmersible floating offshore wind turbine, *Wind Energy* 21 (2018) 70–85.
- [41] Y. Liu, Q. Xiao, A. Incecik, C. Peyrard, D. Wan, Establishing a fully coupled cfd analysis tool for floating offshore wind turbines, *Renewable Energy* 112 (2017) 280–301.
- [42] National Renewable Energy Laboratory, Openfast documentation, 2021. URL: <https://github.com/openfast>, (accessed: 17.08.2021).
- [43] F. Moukalled, L. Mangani, M. Darwish, et al., The finite volume method in computational fluid dynamics, volume 113, Springer, 2016.
- [44] D. C. Wilcox, et al., Turbulence modeling for CFD, volume 2, DCW industries La Canada, CA, 1998.
- [45] F. Menter, Zonal two equation kw turbulence models for aerodynamic flows, in: 23rd fluid dynamics, plasmadynamics, and lasers conference, 1993, p. 2906.
- [46] D. Spalding, Mass transfer through laminar boundary layers—1. the velocity boundary layer, *International Journal of Heat and Mass Transfer* 2 (1961) 15–32.
- [47] D. Spalding, H. Evans, Mass transfer through laminar boundary layers—2. auxiliary functions for the velocity boundary layer, *International Journal of Heat and Mass Transfer* 2 (1961) 199–221.
- [48] F. Liu, A thorough description of how wall functions are implemented in openfoam, *Proceedings of CFD with OpenSource Software* (2016) 1–33.
- [49] M.-C. Hsu, Y. Bazilevs, Fluid-structure interaction modeling of wind turbines: simulating the full machine, *Computational Mechanics* 50 (2012) 821–833.
- [50] S. B. Pope, Turbulent flows, 2001.
- [51] P. E. Farrell, J. R. Maddison, Conservative interpolation between volume meshes by local Galerkin projection, *Computer Methods in Applied Mechanics and Engineering* 200 (2011) 89–100, doi:10.1016/j.cma.2010.07.015.
- [52] P. J. Moriarty, A. C. Hansen, AeroDyn theory manual, Technical Report, National Renewable Energy Lab., Golden, CO (US), 2005.
- [53] E. Gaertner, J. Rinker, L. Sethuraman, F. Zahle, B. Anderson, G. E. Barter, N. J. Abbas, F. Meng, P. Bortolotti, W. Skrzypinski, et al., IEA wind TCP task 37: definition of the IEA 15-megawatt offshore reference wind turbine, Technical Report, National Renewable Energy Lab.(NREL), Golden, CO (United States), 2020.
- [54] A. Robertson, J. Jonkman, M. Masciola, H. Song, A. Goupee, A. Coulling, C. Luan, Definition of the semisubmersible floating system for phase II of OC4, Technical Report, National Renewable Energy Lab.(NREL), Golden, CO (United States), 2014.